ACS Photonics

Article

pubs.acs.org/journal/apchd5

Continuous Wave Resonant Photon Stimulated Electron Energy-Gain and Electron Energy-Loss Spectroscopy of Individual Plasmonic Nanoparticles

Chenze Liu,[†,#] Yueying Wu,[†,‡,#] Zhongwei Hu,[§,#] Jacob A. Busche,[§,#] Elliot K. Beutler,[§] Nicholas P. Montoni,[§] Thomas M. Moore,[∥] Gregory A. Magel,[∥] Jon P. Camden,[‡] David J. Masiello,[*,§] Gerd Duscher,[*,†] and Philip D. Rack[*,†,⊥]

[†]Department of Materials Science and Engineering, University of Tennessee, Knoxville, Tennessee 37996, United States
[‡]Department of Chemistry and Biochemistry, University of Notre Dame, Notre Dame, Indiana 46556, United States
[§]Department of Chemistry, University of Washington, Seattle, Washington 98195, United States
[∥]Waviks Inc., 10330 Markison Road, Dallas, Texas 75238, United States
[⊥]Center for Nanophase Materials Sciences, Oak Ridge National Laboratory, Oak Ridge, Tennessee 37831, United States

Supporting Information

ABSTRACT: The unique optical properties of surface plasmon resonances in nanostructured materials have attracted considerable attention, broadly impacting both fundamental research and applied technologies ranging from sensing and optoelectronics to quantum computing. Electron energy-loss spectroscopy in the transmission electron microscope has revealed valuable information about the full plasmonic spectrum of these materials with nanoscale spatial resolution. Here we report a novel approach for experimentally accessing the photon-stimulated electron energy-gain and stimulated electron energy-loss responses of individual plasmonic nanoparticles via the simultaneous irradiation of a continuous wave laser and continuous current, monochromated electron probe. Stimulated gain and loss probabilities are equivalent and increase linearly in the low-irradiance range of 0.5×10^8 to 4×10^8 W/m^2, above which excessive heating reduces the observed probabilities; importantly in our low-irradiance regime, the photon energy must be tuned in resonance with the plasmon energy for the stimulated gain and loss peaks to emerge. Theoretical modeling based on Fermi's golden rule elucidates how the plasmon resonantly and coherently shuttles energy quanta between the electron probe and the radiation field and vice versa in stimulated electron energy-loss and -gain events. This study opens a fundamentally new approach to explore the quantum physics of excited-state plasmon resonances that does not rely on high-intensity laser pulses or any modification to the EELS detector.

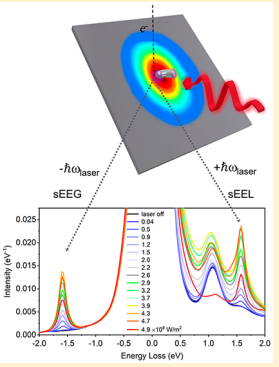

KEYWORDS: *plasmon resonance, electron energy loss (EEL), electron energy gain (EEG), (scanning) transmission electron microscope ((S)TEM), laser*

The ability of nanostructured metals to support plasmon resonances in response to light has implications in many scientific fields and applications such as optoelectronics,[1−3] optical computing,[4,5] and readout strategies for quantum computing.[6,7] Because plasmon excitations are sensitive to their environment, biological and chemical processes can be probed using environment-induced plasmon modulation.[8,9] Plasmons can also transfer electromagnetic energy radiatively,[10] nonradiatively,[11] and/or via hot electron injection and thus can be used to catalyze reactions.[12−14] Due to these, and other, emerging uses, a deeper understanding of plasmon excited states is essential. Electron energy loss spectroscopy in the (scanning) transmission electron microscope ((S)TEM) has been used to gain insight into the physics of plasmonic structures at the nanoscale.[15−17] While theory has facilitated the distinction of bright and dark plasmon modes in more simple structures, distinguishing these modes in complex geometries remains a challenge, as does imaging their photoexcited internal field structure.

Optical pump−probe strategies have long been critical tools to unravel complex materials phenomena. While the probe size typically limits spatial resolution, the temporal domain of pump−probe techniques is virtually unparalleled with sub-femtosecond laser pulses.[18] To push the spatial resolution, over the past two decades optical pumps and focused electron probes have merged into ultrafast electron microscopies (UEMs) with modalities such as diffraction[19,20] and photo-induced near-field electron microscopy (see refs 21−25 for recent perspectives and reviews). For instance, 4D (x, y, z, t) UEM systems utilize photocathodes, which are exposed to short laser pulses to generate electron beamlets (and single

Received: June 9, 2019
Published: August 28, 2019

DOI: 10.1021/acsphotonics.9b00830
ACS Photonics XXXX, XXX, XXX−XXX

electrons) that synchronously arrive at the sample relative to a pulsed laser. Although only a few UEM systems exist worldwide, a wealth of interesting excited-state near-field information has been revealed as described below.

Electron energy gain due to electron/phonon coupling was first observed by Boerch et al. in 1966[26] and more recently in high energy resolution (S)TEM-based electron energy-loss spectroscopy (EELS).[27,28] Photon-stimulated electron energy-gain (sEEG) spectroscopy was first suggested by Howie,[29] and later Garcia de Abajo et al.[30] developed a theoretical framework for sEEG and suggested optical power densities of $\sim 10^{10}$ W/m^2 would be necessary to observe continuous wave (cw) sEEG spectroscopy of gold nanostructures. The allure of sEEG spectroscopy is the possibility of accessing near-field phenomena not limited by the width of the zero loss peak (ZLP) or detector energy resolution, but rather by the spectral resolution of the stimulating optical pump. More recently, Barwick et al.[31] introduced photoinduced near-field electron microscopy (PINEM), which couples an intense laser pulse indirectly to a fast electron probe through the laser-induced evanescent near-field of the target material, thereby generating stimulated electron energy-loss (sEEL) and sEEG signals at discrete multiples of the photon energy ($\pm n\hbar\omega$). They studied the electron energy-gain and stimulated energy-loss spectra of carbon nanotubes and compared them to silver nanorods.[31] The $\sim 10^{14}$ W/m^2, 200 fs pulses produced symmetric gain/loss spectra evidencing photon−plasmon−electron interactions involving up to 8 photon quanta. Later, energy-filtered PINEM maps were used to image the interference of Fabry−Perot-type surface plasmon polariton waves[21] as well as to visualize the channel-like patterns formed in the near-fields of entangled silver nanoparticles.[32] Recently, spectrally resolved PINEM experiments of silver nanorods have confirmed that optical energy resolutions of ~20 meV can be obtained via a tunable light source.[33] Theoretical treatments of photoinduced sEEG have also been developed,[15,34−36] and it was suggested that cw sEEG could be realized with irradiance values on the order of 10^8 W/m^2 for silver nanoparticles, though some have hypothesized[23] that impractically high sample heating would result at these cw irradiances, thus rendering cw sEEG/sEEL unfeasible.

In an attempt to circumvent the need for a photocathode as done in standard PINEM experiments, recently, Das et al.[37] has reported a new method in which a high-power pulsed nanosecond laser (~2 eV photons, 5 ns pulse width, 10 kHz, duty cycle of 5×10^{-3} %, and peak irradiance on the order of 10^{14} W/m^2) is used to expose the sample. sEEL and sEEG peaks at ± 1 and $\pm 2\hbar\omega$ were realized with a modified detector that is synchronized with the laser pulse and only collects electrons that have interacted concurrently with the laser irradiation. Importantly, because they operated in a perturbative regime where no more than one gain event occurs per electron, they realized a resonant mode when the photon energy was tuned to the plasmon peak resonance energy. Furthermore, they overviewed a theory of dissipative quantum evolution and determined the number of photo-excited plasmons generated by the illumination to be on the order of 1.2 in their resonant regime.

As most PINEM experiments have demonstrated, at high enough photon irradiance virtually any photon−target interaction can stimulate loss/gain signals even when the optical transition (plasmonic or not) is weak. For instance, even biological samples have recently been imaged via PINEM.[38,39] Here, through a combination of experiment and theory, we demonstrate a low-irradiance cw regime (10^8 W/m^2) where strong photon−plasmon coupling is critical to observing the sEEL and sEEG signals; in this way, we expect bright plasmon modes to couple stronger than dark plasmon modes. This resonant mode provides the ability to spectrally and spatially map the steady-state near-field of individual plasmonic nanostructures via cw photoexcitation and a continuous electron source in the (S)TEM.

RESULTS AND DISCUSSION

Motivated by these studies and the desire to investigate excited-state phenomena in plasmonic nanomaterials, we leveraged a recently developed optical delivery system that can be attached to any (S)TEM for both photothermal heating[40] and excitation modalities and used it to image the plasmonic responses of individual silver nanoparticles in the weak-field cw limit. The particles are photothermally dewetted from a continuous 30 nm thick silver film (see SI-I for detailed image) using our in situ laser delivery system. Fortuitously, the photothermally dewet nanostructures do not have any silver oxidation because they are generated in high vacuum and provided a distribution of particle shapes and sizes in which to probe for resonance with our laser energy. Figure 1a is a

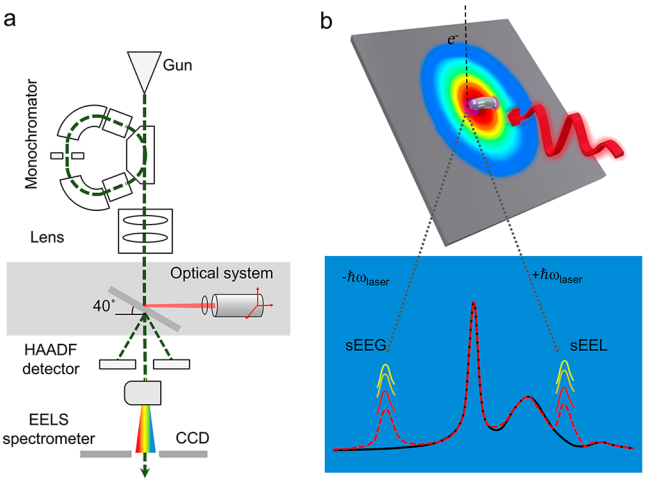

Figure 1. Overview of (S)TEM/EELS and laser system. (a) Schematic of the monochromated (S)TEM/EELS instrument with the optical delivery system mounted orthogonal to the electron beam. (b) Illustration of the coincident and cw focused laser light and 200 keV electron beam; the laser spot has a 3.7 mm radius Gaussian profile and interacts with the sample to produce signature sEEL and sEEG peaks whose intensities vary with laser irradiance.

schematic illustrating the system, developed by Waviks, Inc., attached to a monochromated (S)TEM. The system consists of a laser diode with an emission wavelength of 785 nm and a 1 nm (or 1.4 meV) full-width at half-maximum (fwhm) line width. The tunable laser optical power (up to 215 mW) is coupled to a 5 μm diameter single-mode fiber optic, and the end of the fiber is placed at the focal distance of the lens subsystem, which reimages the fiber-optic end with unit magnification at an approximate working distance of 1 cm. As shown in Figure 1a and b, the unpolarized 3.7 μm radius Gaussian laser spot (at $1/e^2$ irradiance measured at normal incidence and thus slightly elongated due to the tilt) is focused and aligned to the (S)TEM electron coincident point on a 40°

DOI: 10.1021/acsphotonics.9b00830
ACS Photonics XXXX, XXX, XXX−XXX

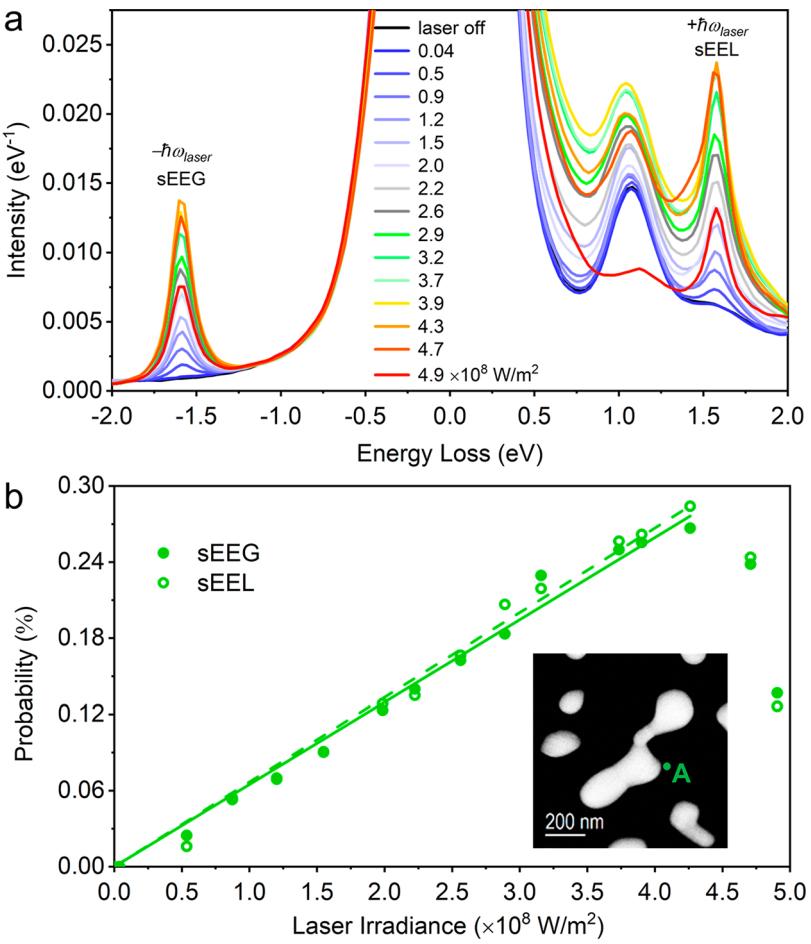

Figure 2. sEEL and sEEG of a silver irregular nanoparticle as a function of laser irradiance. (a) Unprocessed low-loss EEL/EEG point spectra of a photothermally dewetted silver nanoparticle as a function of laser irradiance (×10^8 W/m^2) at the aloof beam position indicated by the green bullet and label A. (b) Integrated sEEG and sEEL probabilities as a function of laser irradiance for the spectra in (a). The solid and dashed lines are linear fits to the sEEG and sEEL data, respectively.

tilted sample via a three-axis nanomanipulator system (see Wu et al. for system details).[40] While all results presented here were operated in cw, the laser can be pulsed down to a several-nanosecond pulse width at up to 16 MHz frequency at a wavelength of 785 nm (1.58 eV). At maximum power and focus, a cw irradiance on the 40° tilted substrate can reach up to ~2 × 10^9 W/m^2.

f2 Figure 2a shows the unprocessed low-loss sEEL/sEEG point spectra of a photothermally dewetted silver nanoparticle (see HAADF (S)TEM image in inset) as a function of laser power at the aloof beam position indicated by position A (see SI-ii for full spectra). Inspection of the EEL spectrum (without laser irradiation) reveals an energy resolution of 0.136 eV as measured by the fwhm of the ZLP. During the experiment, there are slight changes in the ZLP attributed to microscope instabilities and a change in the high-energy side of the background consistent with electron beam induced carbon deposition from prolonged electron exposure. The surface plasmons are clearly visible and no noise reduction or other data enhancement was performed on the spectra. In the laser-irradiated spectra, two additional peaks emerge and are attributed to the sEEL and sEEG peaks at $\pm\hbar\omega_{laser}$, respectively, at ±1.58 eV. For clarity we plot the data using standard EELS convention so the sEEG signature is at negative electron energy loss.

For the zero-irradiance spectra (laser off), there are two plasmon peaks in this low-loss region of interest: one centered at ~1.05 eV and another small peak centered near the laser wavelength 1.48 eV. Detailed peak fitting of the spectra was performed to analyze the full low-loss/gain spectra (see SI-iii for details). Notably, the average fwhm of the sEEL and sEEG peak fits (0.136 ± 0.0089 eV) match well with the fwhm of the ZLP.

Figure 2b is a plot of the integrated sEEG and sEEL probabilities as a function of laser irradiance for the spectra in Figure 2a. Interestingly, the EEL spectrum in Figure 2a at zero laser irradiance has only a small plasmon peak near the 1.58 eV laser energy; however, the laser couples strongly to this apparent bright mode, which also interacts with the field of the swift (<500 attosecond interaction time) passing STEM electron, as evidenced by the strong sEEL and sEEG peaks in the spectrum. Notably, the sEEL and sEEG peaks increase approximately linearly as a function of laser irradiance in the range of 8.8 × 10^7 to 4.3 × 10^8 W/m^2. Consistent with previous PINEM results[31,32] and as discussed below in our modeling results, the sEEL and sEEG peak intensities have approximately the same integrated probability. Note that because of the relatively low cw laser irradiance values relative to PINEM, only single quantum exchanges of energy between the laser, target, and electron beam are observed, as no multiphoton sEEL and sEEG responses are detected. Addi-

DOI: 10.1021/acsphotonics.9b00830
ACS Photonics XXXX, XXX, XXX−XXX

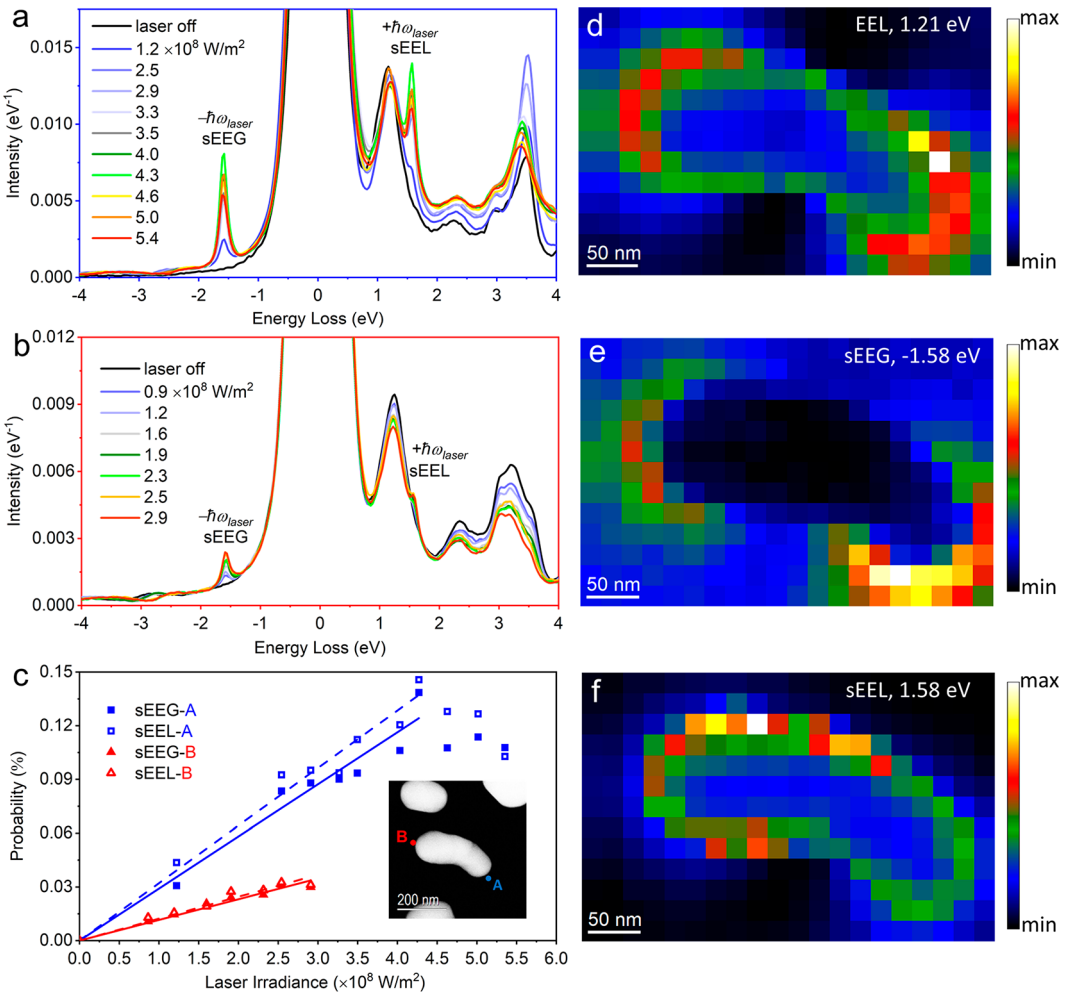

Figure 3. sEEL and sEEG of a silver rod-like nanoparticle as a function of laser irradiance. Unprocessed low-loss EEL spectra of silver rod-like structures at (a) position A and (b) position B as a function of laser irradiance ($\times 10^8$ W/m^2) at the aloof beam position. The positions A and B are indicated in the inset of (c). (c) Integrated sEEG and sEEL probabilities as a function of laser irradiance. The solid (sEEG) and dashed (sEEL) lines are linear fits for the data obtained at position B (blue) and C (red), respectively. The solid and dashed lines are linear fits to the sEEG and sEEL data, respectively. EEL maps of (d) the 1.21 eV dipole peak at zero irradiance, (e) −1.58 eV sEEG map, and (f) the +1.58 eV sEEL map, both at 2×10^8 W/m^2 irradiance.

tionally, and consistent with the lower irradiance, there is no detectable change in the ZLP intensity. Interestingly, both peak intensities decrease at irradiance values of $>4.3 \times 10^8$ W/m^2, which is attributed to photothermal heating of the silver nanostructure, which is known to damp plasmons and shift the resonance to lower energy. Anecdotally, when the laser is increased slightly to 5×10^8 W/m^2, the silver nanostructures studied evaporate completely (see SI-iv for images). Furthermore, the broad plasmon modes associated with the electron-beam-induced carbon deposition also concurrently decrease in the $>4.3 \times 10^8$ W/m^2 irradiance region.

Figure 3a and b show the point spectra as a function of irradiance at the aloof positions of the rod-like structure shown in the inset of Figure 3c (see SI-ii for full low-loss spectra); again no data processing was performed for the spectra. Figure 3c is a plot of the integrated sEEL and sEEG probabilities as a function of irradiance taken at these two positions (ignoring the spontaneous EEL contribution convoluted on the loss side); note the sEEL and sEEG probabilities are again comparable for each position. The rod has approximate dimensions of ∼330 nm long, an average width of ∼120 nm, and average height of ∼100 nm (assuming an equilibrium wetting angle for the trans-axial dimension of 135 degrees). At the aloof positions at the rod ends, the spectra consist of peaks associated with the longitudinal dipole (1.21 eV), longitudinal quadrupole (2.3 eV), and several higher energy (>3 eV) modes including the transverse dipole among higher order modes. Note the intensity of the higher order mode peak at ∼3.5 eV varies in the unprocessed data, which has contributions from carbon deposition (and removal at higher irradiance) and likely slight electron beam mispositioning over the duration of the experiment. No multiphoton sEEL is contributing, as evidenced by the energy-gain region having no peaks at $-2\hbar\omega_{laser}$ = 3.16 eV. Figure 3d illustrates the 1.21 eV dipole mode EELS map at zero irradiance, which has the expected high probability distribution at the rod ends (see SI-v for complementary 2.3 eV quadrupole mode map). Figure 3e and f are the associated sEEG and sEEL probability maps, respectively, when exposed to an irradiance of $\sim 2 \times 10^8$ W/m^2. The sEEG probability map is consistent with the longitudinal dipole map, which suggests good coupling to this bright mode despite the laser energy being detuned ∼0.37 eV to higher energy from the dipole plasmon resonance. As the spectra illustrate in Figure 3a and b and the longitudinal

DOI: 10.1021/acsphotonics.9b00830
ACS Photonics XXXX, XXX, XXX−XXX

dipole map suggests in Figure 3d, the EEL probability is slightly higher on the right side of the rod, and thus concomitantly the sEEG and sEEL probabilities are slightly higher on the right-hand side of the rod. For position A, where relatively higher laser powers were explored, the sEEL and sEEG probabilities decrease when the irradiance exceeded ~4 $\times 10^8$ W/m^2, and the silver nanostructure evaporated when the irradiance exceeded 5.4 $\times 10^8$ W/m^2 (see image in SI-vi).

According to Das et al.,[37] at low laser intensities where the stimulated sEELS and sEEGS intensities are on the order of the spontaneous EELS intensity, the mean number of stimulated plasmons (M) can be deduced by taking a ratio of the spontaneous plus stimulated loss intensity to the stimulated gain intensity, where this ratio is equal to $(M + 1)/M$. Based on the deconvolved spectra that includes only the longitudinal dipole peak (at 1.2 eV) and the stimulated gain (at −1.58 eV) and loss (at 1.58 eV) peaks, the experimental peak integrated intensities were determined from Figure 3a spectra collected at 1.2, 2.5, and 4 $\times 10^8$ W/m^2 irradiance. The experimental ratios were determined to be 24.1, 10.5, and 8.7, respectively; thus the mean number of photoexcited plasmons at these irradiances were estimated to be 0.04, 0.10, and 0.13, respectively.

Due to the weak interaction of light with matter and the low cw laser intensity and (S)TEM electron current used herein, the spectral signatures of sEEL and sEEG can be well understood using time-dependent perturbation theory up to second order in electron−plasmon and photon−plasmon interactions. Each of these interactions either reduce or increase the (S)TEM electron momentum from $\hbar k_i$ to $\hbar k_f = \hbar k_i - \hbar q$, with $\hbar q$ being a small ($|\hbar q| \ll \hbar k_i$) transfer momentum that is positive in energy-loss events and negative in energy-gain events.

In both cases, the cw laser and nanoparticle plasmons are assumed to have reached a steady state prior to the electron−plasmon interaction. Additionally, we choose the initial population $M_\lambda(\omega) = M_\lambda^{\max}\frac{\gamma_{\text{laser}}^2}{(\omega-\omega_{\text{laser}})^2+\gamma_{\text{laser}}^2}$ of each plasmon state λ to be frequency-dependent to model the excitation of a continuous plasmon density of states by a laser of line width γ_{laser} and peak frequency ω_{laser}. Letting the laser polarization and longitudinal dipole plasmon be oriented along the x-axis, the longitudinal plasmon occupation number is $M_x(\omega) \geq 0$ such that the initial state of the three dipole plasmons is $|M_x(\omega),0_y,0_z\rangle$, with the occupation numbers of the undriven transverse (y, z) plasmons taken to be zero. The initial state of the laser-populated photon field is given by the collective photon state $|\{N\}\rangle = |\ ..., N_\alpha, N_{\alpha'}, N_{\alpha''}, ...\rangle$, with α the collective index of each photon mode and N_α the occupation number of the αth photon mode. Additionally, the initial state of the (S)TEM electron, whose motion along directions perpendicular to its propagation axis can be safely neglected for sufficiently small q, is well-approximated as a box-quantized, one-dimensional free particle with a wave function $\langle \boldsymbol{r}|k_i\rangle = \phi_R(\boldsymbol{R})\exp(ik_iz)/\sqrt{L}$. Here, $\boldsymbol{R}$ is the cylindrical radial vector and $|\phi_R(\boldsymbol{R})|^2 \approx \delta(\boldsymbol{R} - \boldsymbol{R}_0)$, with $\boldsymbol{R}_0$ being the impact parameter of the electron.[36] To be consistent with the definition of the photon field, the electron wave function is described in second quantization (see SI-vi) as $|k_i\rangle = |\ ..., 0, 1_{k_i}, 0, ...\rangle$, with all modes having an occupation number of zero except the k_i^{th} state of momentum $\hbar k_i$, which has an occupation number of one.

Collectively, the initial state of the system is then $|i\rangle = |\ k_i, \{N\}, \{M_x(\omega),0_y,0_z\}\rangle$, and the allowed final states are determined by the electron−plasmon and photon−plasmon coupling, $\hat{H}_{\text{el-pl}} = -\hat{\mathbf{d}}\cdot\hat{\mathbf{E}}_{\text{el}} = \sum_{kk'\lambda}(g_{k'k\lambda}\hat{c}_k^\dagger\hat{c}_k\hat{b}_\lambda^\dagger + g_{k'k\lambda}^*\hat{c}_k^\dagger\hat{c}_{k'}\hat{b}_\lambda)$ and $\hat{H}_{\text{ph-pl}} = -\hat{\mathbf{d}}\cdot\hat{\mathbf{E}}_{ph} = \sum_{\alpha\lambda}g_{\alpha\lambda}(\hat{b}_\lambda^\dagger\hat{a}_\alpha - \hat{b}_\lambda\hat{a}_\alpha^\dagger)$, with $\lambda = x, y, z$ labeling the three nanoparticle dipole plasmons and $\hat{\mathbf{E}}_{el}$ and $\hat{\mathbf{E}}_{ph}$ being the time-dependent electric field operators of the electron and photon fields. Here, $\hat{\mathbf{d}} = \sum_\lambda d_\lambda(\hat{b}_\lambda + \hat{b}_\lambda^\dagger)\mathbf{e}_\lambda$ is the transition dipole operator of the dipole plasmon modes of the rod with $\hat{b}_\lambda$ being the annihilation operator of the dipole plasmon oriented in the λ-direction, denoted by the unit vector $\mathbf{e}_\lambda$. Analogously, $\hat{a}_\alpha$ and $\hat{c}_k$ are the annihilation operators of the αth photon mode and kth electron mode, respectively. The coupling strengths

$$g_{k'k\lambda} = -\frac{2e|k'-k|d_\lambda}{\gamma^2 L}\kappa_\lambda\left(\frac{|k'-k|R_0}{\gamma}\right)$$

and

$$g_{\alpha\lambda} = -i\sqrt{\frac{2\pi\hbar\omega_\alpha}{V}}\,d_\lambda(\mathbf{e}_\lambda\cdot\boldsymbol{\epsilon}_\alpha)$$

in which

$$\kappa_{x,y}\left(\frac{|k'-k|R_0}{\gamma}\right) = -\gamma K_1\left(\frac{|k'-k|R_0}{\gamma}\right)\frac{\mathbf{R}_0\cdot\mathbf{e}_{x,y}}{R_0}$$

and

$$\kappa_z\left(\frac{|k'-k|R_0}{\gamma}\right) = -i\frac{k'-k}{|k'-k|}K_0\left(\frac{|k'-k|R_0}{\gamma}\right)$$

depend upon the radiation mode frequencies ω_α, polarizations $\boldsymbol{\epsilon}_\alpha$, and quantization volume V, as well as the Lorentz contraction factor γ and quantization length L (see SI-vi).

Inspection of the different allowed time orderings of $\hat{H}_{\text{el-pl}}$ and $\hat{H}_{\text{ph-pl}}$ within the calculation of a second-order transition rate from $|i\rangle = |\ k_i, \{N\}, \{M_x(\omega),0_y,0_z\}\rangle$, to $|f\rangle = |\ k_f, \{N'\}, \{M'_x(\omega), M'_y, M'_z\}\rangle$, reveals that only four second-order scattering processes contribute: the plasmon may gain (simultaneous plasmon excitation (SPE)) or lose (simultaneous plasmon deexcitation (SPD)) two quanta of energy during the interaction, or it may simply mediate energy transfer from the photon field to the electron probe (stimulated electron energy-gain (sEEG)) or vice versa (stimulated electron-induced emission of radiation (sEIRE)).

Of the four processes, only SPE and sEIRE can contribute to the total loss signal. As SPE is the stimulated analog of the more commonly known EEL process, one might expect its contribution to the loss signal to be of prime importance. The transition rate for SPE is given by

DOI: 10.1021/acsphotonics.9b00830
ACS Photonics XXXX, XXX, XXX−XXX

$$w^{(2)}_{\mathrm{SPE}} = \frac{2\pi}{\hbar}\left|\sum_{m}\frac{\langle k_f, \{..., N_\alpha - 1, ...\}, \{M_x(\omega) + 2, 0_y, 0_z\}|\hat{H}_{\mathrm{el-pl}}|m\rangle\langle m|\hat{H}_{\mathrm{ph-pl}}|k_i, \{N\}, \{M_x(\omega), 0_y, 0_z\}\rangle}{E_i - E_m} + \sum_{m'}\frac{\langle k_f, \{..., N_\alpha - 1, ...\}, \{M_x(\omega) + 2, 0_y, 0_z\}|\hat{H}_{\mathrm{ph-pl}}|m'\rangle\langle m'|\hat{H}_{\mathrm{el-pl}}|k_i, \{N\}, \{M_x(\omega), 0_y, 0_z\}\rangle}{E_i - E_{m'}}\right|^2 \delta(E_f - E_i) \quad (1)$$

wherein the first term describes the properly time-ordered single-electron and single-photon interaction with the initial plasmon state $|\{M_x(\omega), 0_y, 0_z\}\rangle$, leaving the (S)TEM electron decelerated ($q > 0$) by interaction with the excited surface plasmon. The second represents the improper time ordering of the two interactions, in which the electron scattering precedes the absorption of a photon. While not intuitive, the fact that both time orderings contribute to this scattering process (as opposed to the strictly causal interactions) has been discussed extensively in the literature.[41−43] Remarkably, the addition of the two oppositely time-ordered terms in eq 1 (see SI-vi) results in a transition rate of zero. As a result, the second-order contribution to the total loss signal is completely determined by the rate of the sEIRE process as demonstrated below (see also SI-vi), with SPE providing no contribution.

Analyzing the two possible gain processes, SPD and sEEG, one can show that the transition rate of SPD,

$$w^{(2)}_{\mathrm{SPD}} = \frac{2\pi}{\hbar}\left|\sum_{m}\frac{\langle k_f, \{..., N_\alpha + 1, ...\}, \{M_x(\omega) - 2, 0_y, 0_z\}|\hat{H}_{\mathrm{el-pl}}|m\rangle\langle m|\hat{H}_{\mathrm{ph-pl}}|k_i, \{N\}, \{M_x(\omega), 0_y, 0_z\}\rangle}{E_i - E_m} + \sum_{m}{}',\frac{\langle k_f, \{..., N_\alpha + 1, ...\}, \{M_x(\omega) - 2, 0_y, 0_z\}|\hat{H}_{\mathrm{ph-pl}}|m'\rangle\langle m'|\hat{H}_{\mathrm{el-pl}}|k_i, \{N\}, \{M_x(\omega), 0_y, 0_z\}\rangle}{E_i - E_{m'}}\right|^2 \delta(E_f - E_i) \quad (2)$$

is also zero by similar reasoning (see SI-vi). Therefore, the second-order contributions to the total loss and gain signals are entirely described by the transition rates $w^{(2)}_{\mathrm{sEIRE}}$ and $w^{(2)}_{\mathrm{sEEG}}$, respectively, which describe the likelihood that the (S)TEM electron and a photon will interact simultaneously with the plasmon, causing a deceleration and acceleration of the electron, respectively. These transition rates can be calculated as

$$w^{(2)}_{\mathrm{sEIRE}} = \frac{2\pi}{\hbar}\left|\sum_{m}\frac{\langle k_f, \{..., N_\alpha + 1, ...\}, \{M_x(\omega), 0_y, 0_z\}|\hat{H}_{\mathrm{el-pl}}|m\rangle\langle m|\hat{H}_{\mathrm{ph-pl}}|k_i, \{N\}, \{M_x(\omega), 0_y, 0_z\}\rangle}{E_i - E_m} + \sum_{m}{}',\frac{\langle k_f, \{..., N_\alpha + 1, ...\}, \{M_x(\omega), 0_y, 0_z\}|\hat{H}_{\mathrm{ph-pl}}|m'\rangle\langle m'|\hat{H}_{\mathrm{el-pl}}|k_i, \{N\}, \{M_x(\omega), 0_y, 0_z\}\rangle}{E_i - E_{m'}}\right|^2 \delta(E_f - E_i) \quad (3)$$

and

$$w^{(2)}_{\mathrm{sEEG}} = \frac{2\pi}{\hbar}\left|\sum_{m}\frac{\langle k_f, \{..., N_\alpha - 1, ...\}, \{M_x(\omega), 0_y, 0_z\}|\hat{H}_{\mathrm{el-pl}}|m\rangle\langle m|\hat{H}_{\mathrm{ph-pl}}|k_i, \{N\}, \{M_x(\omega), 0_y, 0_z\}\rangle}{E_i - E_m} + \sum_{m}{}',\frac{\langle k_f, \{..., N_\alpha - 1, ...\}, \{M_x(\omega), 0_y, 0_z\}|\hat{H}_{\mathrm{ph-pl}}|m'\rangle\langle m'|\hat{H}_{\mathrm{el-pl}}|k_i, \{N\}, \{M_x(\omega), 0_y, 0_z\}\rangle}{E_i - E_{m'}}\right|^2 \delta(E_f - E_i) \quad (4)$$

with $k_f < k_i$ in $w^{(2)}_{\mathrm{sEIRE}}$ and $k_f > k_i$ in $w^{(2)}_{\mathrm{sEEG}}$. It is straightforward to show that the second-order sEEG transition rate recovers the same result given in ref 36 with $M_x(\omega) \to 0$, as the second (improper) term of eq 4 becomes zero. However, even at finite $M_x(\omega)$, both $w^{(2)}_{\mathrm{sEEG}}$ and $w^{(2)}_{\mathrm{sEIRE}}$ turn out to be independent of the initial plasmon occupation number (see SI-vi) and $w^{(2)}_{\mathrm{sEEG}}$ agrees with previous work for any $M_x(\omega)$. It is also important to note that even though sEIRE photons are not detected in our experiment, eq 3 nonetheless shows that the loss signatures of the sEIRE process are encoded in the final electron energy spectrum.

In addition to the second-order contributions to the total loss rate, the fast electron probe can also lose or gain energy by interacting with the laser-excited plasmon mode *without* the simultaneous creation or destruction of a photon. The rates of these phenomena are calculated at first order. In the case of energy loss, the electron can further lose energy to modes beyond those that are pumped by the laser such that the total first-order energy loss rate of all three plasmons is

DOI: 10.1021/acsphotonics.9b00830
ACS Photonics XXXX, XXX, XXX−XXX

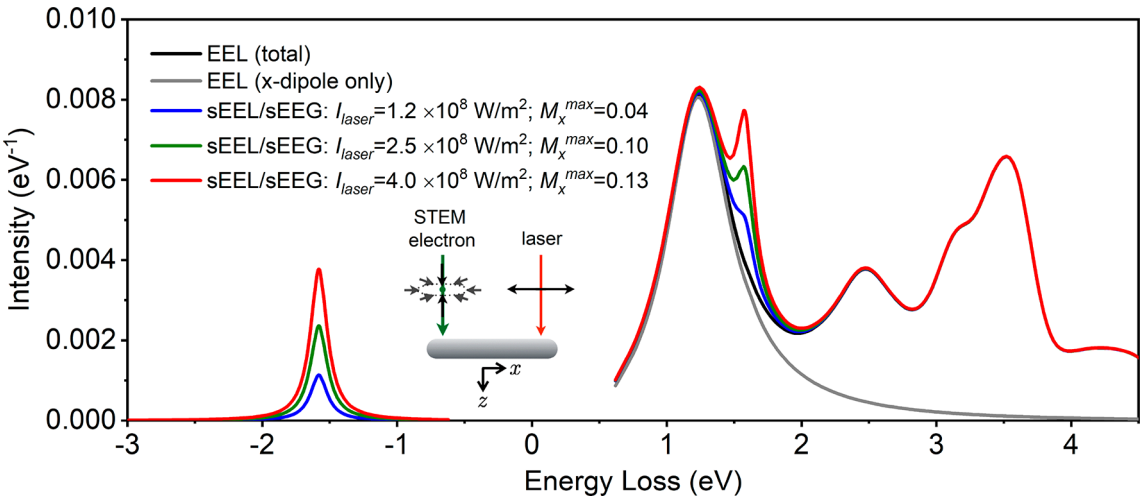

Figure 4. Computed total loss and gain spectra of a silver nanorod interacting with the pair of co-propagating cw laser and STEM-electron beams illustrated in the inset. The simulated EEL spectrum is also shown for reference and is the limiting behavior of the sEEL signal when the laser field is removed. The sEEL and sEEG profiles are symmetrically distributed at $\pm\hbar\omega_{laser} = \pm 1.58$ eV and, after subtracting the EEL spectral profile, are otherwise of equal amplitude up to a factor of $(N+1)/N$. The sEEL and sEEG spectra were calculated with an electron beam impact parameter of 107 nm and a plasmon effective mass of 1.6×10^{-34} g. Additionally, the theoretical curves were calculated with a maximum plasmon occupation number of M_x^{max} of 0.04, 0.10, and 0.13, which are extracted from the measured I_{laser} = 1.2, 2.5, and 4.0 × 10^8 W/m^2 spectra in Figure 3 together with eqs 7 and 8. Finally, all curves were convolved with a normalized Lorentzian distribution with a fwhm of 150 meV to model the finite energy resolution of the instrument.

$$w_{EEL} + w_{sEEL}^{(1)} = \sum_{\lambda} \frac{2\pi}{\hbar} |\langle k_f, \{N\}, \{..., M_\lambda(\omega) + 1, ...\}|$$
$$\hat{H}_{el-pl} |k_i, \{N\}, \{M_x(\omega), 0_y, 0_z\}\rangle|^2 \delta(E_f - E_i)$$

with w_{EEL} the well-known spontaneous EEL rate and $w_{sEEL}^{(1)}$ the first-order stimulated EEL rate (SI-vi). Therefore, $w_{sEEL}^{(1)}$ and w_{EEL} must be added to $w_{sEIRE}^{(2)}$ to reconstruct the total loss spectrum measured in our experiment.

Similarly, the total first-order contribution to the gain rate is

$$w_{sEEG}^{(1)} = \frac{2\pi}{\hbar} |\langle k_f, \{N\}, \{M_x(\omega) - 1, 0_y, 0_z\}| \hat{H}_{el-pl}$$
$$|k_i, \{N\}, \{M_x(\omega), 0_y, 0_z\}\rangle|^2 \delta(E_f - E_i)$$

which, in contrast to the first-order loss rate, contains no spontaneous contributions. It is thus clear that the total gain signal, $w_{sEEG}^{(1)} + w_{sEEG}^{(2)}$, is entirely caused by the sEEG process, allowing the label "total gain" to be dropped. Similarly on dropping the label "total loss" in favor of sEEL now that all loss processes are accounted for, the sEEL and sEEG functions can be expressed in the following intuitive forms (see SI-vi),

$$\Gamma_{sEEL}(\omega) \approx \Gamma_{EEL}(\omega) + \left(M_x(\omega) + \frac{\pi}{2\hbar\omega_x}\sigma_x(\omega_x)\mathcal{I}(\omega)\right)\Gamma_{EELx}(\omega) \quad (5)$$

and

$$\Gamma_{sEEG}(\omega) = \left(M_x(-\omega) + \frac{\pi}{2\hbar\omega_x}\sigma_x(\omega_x)\mathcal{I}(-\omega)\right)\Gamma_{EELx}^{(-)}(\omega) \quad (6)$$

which are simply related to the sum of the individual rates[36] over the full spectrum of possible final states of the electron probe and photon field and are expressed in units of percent per unit loss/gain energy. Specifically, $\Gamma_{EELx}(\omega)$ is a measure of EEL to *only* the longitudinal dipole plasmon with natural frequency $\Omega_x = \omega_x - i\gamma_x(\omega)$, while $\Gamma_{EEL}(\omega)$ is simply the sum of the EEL contributions from all three dipolar plasmons modes. $\mathcal{I}(\omega)$ is the spectral intensity, measured in units of intensity per unit frequency of the cw laser source and $\sigma_x(\omega)$ is the extinction cross section of the longitudinal dipole plasmon. In eq 6, the superscript $(-)$ indicates that the EELx function of eq 5 has been reflected across $\omega = 0$ such that the sEEG signal appears at negative frequencies. Explicitly,

$$\Gamma_{EELx}(\omega) = \frac{4e^2\omega^2}{\pi\hbar^2 v^4 \gamma^4}\left[\frac{\gamma^2(\mathbf{R}_0\cdot\mathbf{e}_x)^2}{R_0^2} K_1^2\left(\frac{|\omega|R}{v\gamma}\right)\right] \mathrm{Im}\{\alpha_x(\omega)\}$$

with $\alpha_x(\omega) = d_x^2/(\hbar\Omega_x - \hbar\omega)$; the expression for $\Gamma_{EELx}^{(-)}(\omega)$ can then be acquired by letting $\omega \to -\omega$.

For sufficiently narrow laser line widths, eqs 5 and 6 can be simplified by letting

$$\mathcal{I}(\omega)\Gamma_{EELx}(\omega) \to I_{laser}\frac{1}{\pi}\frac{\gamma_{laser}}{(\omega - \omega_{laser})^2 + \gamma_{laser}^2}\Gamma_{EELx}(\omega_{laser})$$

and

$$\mathcal{I}(-\omega)\Gamma_{EELx}^{(-)}(\omega) \to I_{laser}\frac{1}{\pi}\frac{\gamma_{laser}}{(-\omega - \omega_{laser})^2 + \gamma_{laser}^2}\Gamma_{EELx}^{(-)}(-\omega_{laser})$$

respectively, with I_{laser} the peak laser irradiance, giving (see SI-vi)

$$\Gamma_{sEEL}(\omega) \approx \Gamma_{EEL}(\omega) + M_x(\omega)\Gamma_{EELx}(\omega) + \left(\frac{\sigma_x(\omega_x)I_{laser}}{2\hbar\omega_x}\frac{N+1}{N}\frac{\gamma_{laser}}{(\omega - \omega_{laser})^2 + \gamma_{laser}^2}\right)\Gamma_{EELx}(\omega_{laser}) \quad (7)$$

and

$$\Gamma_{sEEG}(\omega) \approx M_x(-\omega)\Gamma_{EELx}^{(-)}(\omega) + \frac{\sigma_x(\omega_x)I_{laser}}{2\hbar\omega_x}\frac{\gamma_{laser}}{(-\omega - \omega_{laser})^2 + \gamma_{laser}^2}\Gamma_{EELx}^{(-)}(-\omega_{laser}) \quad (8)$$

Here N is the occupation number of the single cw laser mode modeled in the narrow-width limit. Note that for large N, the

DOI: 10.1021/acsphotonics.9b00830
ACS Photonics XXXX, XXX, XXX−XXX

sEEL and sEEG functions become equivalent, up to the magnitude of the EEL signal, at each $\pm\omega$. Note also that sEEL reduces to EEL, while sEEG vanishes in the limit where the laser irradiance (and therefore $M_x(\omega)$) is reduced to zero. These expressions, while approximate, make explicit the dependence of sEEL and sEEG upon optical extinction and EELS and provide a simple route to computing sEEL and sEEG spectra using continuum optical and electron scattering codes such as the DDA,[44,45] MNPBEM,[46] and e-DDA.[47,48]

Figure 4 shows the theoretical sEEL, sEEG, and EEL spectra calculated for a 321 × 120 × 120 nm^3 silver nanorod lying on a SiO_2 substrate in a vacuum. Here, the electron beam and laser field co-propagate down an axis that is oriented normal to the long axis of the nanorod (see inset). The spectra are convolved pointwise with a normalized Lorentzian distribution of variance determined by the width of the ZLP (150 meV). Subtraction of the EEL spectrum from the sEEL spectrum would show that the stimulated gain and loss functions are nearly equivalent in amplitude as noted previously[36] with the difference arising only from the ratio $(N + 1)/N$ that appears in $w^{(2)}_{\mathrm{sEIRE}}$. In the limit of large laser occupation numbers ($N + 1 \approx N$), integration of the experimental sEEL and sEEG spectra of Figure 3 as well as the theory given in eqs 7 and 8 between 0 and ±2 eV allows for the inference of $M_x^{\max}$. For peak laser intensities of 1.2, 2.5, and 4.0 × 10^8 W/m^2, the inferred maximum plasmon occupation numbers are 0.04, 0.10, and 0.13, respectively. Comparison of Figures 4 and 3a highlights the remarkable quantitative agreement between the sEEG and sEEL peaks of experiment and theory. This supports the idea that the low-intensity cs laser used in our experiment only weakly populates the nanoparticle plasmon mode, yet we are still able to measure gain signal.

The experimental demonstration and theoretical underpinnings of low-irradiance laser sEEL and sEEG illustrated here are an exciting first step in co-continuous electron and photon photoinduced near-field electron microscopy using a monochromated STEM and high-resolution EELS. To extend the optical power range, higher thermal conductivity and smaller membranes could be used to enhance heat dissipation at high irradiance. Furthermore, multispectral cw photoexcited sEEL and sEEG would be possible by coupling other laser diode wavelengths to the single-mode fiber, a project that is now underway. For instance, while EELS conveniently has access to the entire plasmonic spectrum, the combination of EELS and multispectral low-irradiance photoexcited sEEL and sEEG could distinguish between optically bright and dark modes as well as the excited-state internal field structure of the former. Thus, we envision that the near-field optical phenomena previously only visible with highly specialized UEMs will be accessible with a standard (S)TEM system equipped with the cw optical delivery source.[40]

CONCLUSION

In summary, we have demonstrated stimulated electron energy-loss and stimulated electron energy-gain spectroscopy with a continuous wave laser source and monochromated electron source in a (S)TEM. These signatures emerge at an irradiance value of ∼5 × 10^7 W/m^2 and increase approximately linearly to ∼5 × 10^8 W/m^2. Above this irradiance range, photothermal heating causes the sEEG and sEEL probability to decrease. sEEL and sEEG mapping of a rod-like silver nanostructure confirms that 1.58 eV photons couple to the bright longitudinal dipole plasmon mode. Analytical modeling of the simultaneous (S)TEM electron− and cw laser photon−plasmon interactions based on time-dependent perturbation theory demonstrates the connection between the total loss and gain spectra and the more intuitive optical extinction, laser intensity, and normal EEL spectrum. By exploiting this connection, model simulations of the sEEL and sEEG of an individual silver nanorod elucidate the fundamental processing underlying our experimental observations. The ability to visualize the field structure of excited-state plasmons opens up new directions for optically stimulated fast electron spectroscopy of electronically excited nanomaterials, such as, the direct testing of optoelectronic circuits. One can also imagine that, coupled with a gas cell, plasmon-based sensors and catalytic reactions can be synchronously imaged and correlated to those modes that are bright. Importantly, the photon delivery instrument used in this study can be attached to practically any microscope and equipped with various light sources, thus providing a more universal approach to visualizing atomic scale near-field phenomena that are critical to many photonic applications.

METHODS

Sample Preparation. An ∼25 nm silver film was RF magnetron sputter deposited directly onto 20 nm SiO_2 membranes (TEMwindows.com, a division of SiMPore Inc., Rochester, NY, USA). The silver film was sputtered at 20 W RF power, 25 standard cubic cm per minute Ar flow, and 5 mTorr chamber pressure.

Experimental Apparatus. A new photon delivery system was mounted on the monochromated Carl Zeiss LIBRA 200MC (S)TEM, as shown schematically in Figure 1. The optical delivery setup and laser information were elaborated in our previous work.[40] Peak powers up to >200 mW can be delivered to the sample from a 785 nm wavelength laser diode system coupled through a 5 μm single-mode fiber. The laser is gated by a software-controlled pulse generator that can vary the laser pulse width from a few nanoseconds to cw at repetition rates up to 16 MHz.

EELS Experiments. The TEM was operated at 200 kV in (S)TEM mode with a camera length of 945 mm. The collection semiangle (β) was 45 mrad, and the convergence semiangle (α) was 10 mrad. The low-loss spectra were collected with a monochromator slit of 0.5 μm, and a dispersion of 30 meV per channel was chosen for the spectrometer acquisition. The average energy resolution (defined as the full width at half-maximum of the zero-loss peak) was measured to be 136 meV for a summed spectrum; the energy spread for all single and summed spectra collected was between 120 and 150 meV. For each low-loss point spectrum, 10 frames with a dwell time of 0.1 s each were summed up to yield high count values and signal-to-noise ratios. The average energy resolution (defined as the full width at half-maximum of the zero-loss peak) was measured to be 136 meV. For the EELS map acquisition, a region of interest with 20 × 13 pixel spectra (1 pixel ∼19.5 nm × 19.5 nm) is defined over the entire silver nanoparticle. The pixel dwell time for each pixel in the EEL maps is 0.3 s. The maps of the sEEG (−1.58 eV), sEEL (1.58 eV), 1.21 eV dipole mode, and the 2.3 eV quadrupole mode are generated using the Gatan Digital Micrograph software by plotting spectra intensity in designated energy slices within the 3D spectrum image data cube (x, y, energy-loss).

DOI: 10.1021/acsphotonics.9b00830
ACS Photonics XXXX, XXX, XXX−XXX

■ ASSOCIATED CONTENT

Supporting Information

The Supporting Information is available free of charge on the ACS Publications website at DOI: 10.1021/acsphotonics.9b00830.

STEM image of the dewet silver film, full low-loss electron energy loss spectra, peak fitting description and tabular data, STEM images before and after high laser fluence exposure, EELS map of the quadrupole mode of the rod-like structure from Figure 3 and representative point spectra from the map, detailed theoretical description of sEEL and sEEG modeling, detailed peak fitting script and procedure (PDF)

■ AUTHOR INFORMATION

Corresponding Authors

*E-mail: masiello@chem.washington.edu.
*E-mail: gduscher@utk.edu.
*E-mail: prack@utk.edu.

ORCID

Chenze Liu: 0000-0001-6599-1616
Yueying Wu: 0000-0003-4345-2771
Zhongwei Hu: 0000-0002-2783-7981
Jacob A. Busche: 0000-0003-4797-9415
Jon P. Camden: 0000-0002-6179-2692
David J. Masiello: 0000-0002-1187-0920
Philip D. Rack: 0000-0002-9964-3254

Author Contributions

#C. Liu, Y. Wu, Z. Hu, and J. A. Busche are co-first authors.

Author Contributions

C.L. and Y.W. performed the laser/(S)TEM/EELS experiments under the direction of P.D.R. and G.D. P.D.R., G.D., J.P.C, Y.W., and C.L. collaborated on the interpretation of the experimental results. C.L. and G.D. did the majority of the computer analysis of the experimental data. T.M.M. and G.A.M. designed and built the laser delivery system. Z.H., J.A.B., E.K.B., and N.P.M. formulated the theoretical model and performed numerical simulations with help from D.J.M. P.D.R., G.D., Z.H., C.L., J.A.B., and D.J.M. wrote the paper with contributions from all coauthors.

Notes

The authors declare no competing financial interest.

■ ACKNOWLEDGMENTS

P.D.R. and Y.W. acknowledge the experimental plasmon/EELS study support by NSF DMR-1709275 and 1709601. P.D.R., T.M.M., and G.A.M. acknowledge NSF SBIR-1721719 for the laser delivery system support. C.L. and G.D. acknowledge the U.S. Department of Energy, Office of Science, Basic Energy Sciences (BES), Materials Sciences and Engineering Division, for support of the EELS analysis. J.P.C. acknowledges support from the U.S. Department of Energy Basic Energy Sciences under Award Number DE-SC0018169. The theoretical modeling was supported by the U.S. Department of Energy Basic Energy Sciences under Award Number DE-SC0018040 (D.J.M.) and the numerical simulations (D.J.M.) supported by NSF DMR1708189. The numerical simulations were facilitated through the use of advanced computational, storage, and networking infrastructure provided by the Hyak supercomputer system at the University of Washington. P.D.R. and G.D. acknowledge Sergei V. Kalinin for valuable technical discussions.

■ REFERENCES

(1) Cheben, P.; Halir, R.; Schmid, J. H.; Atwater, H. A.; Smith, D. R. Subwavelength Integrated Photonics. *Nature* **2018**, *560*, 565−572.

(2) Salerno, M.; Krenn, J. R.; Lamprecht, B.; Schider, G.; Ditlbacher, H.; Félidj, N.; Leitner, A.; Aussenegg, F. R. Plasmon Polaritons in Metal Nanostructures: The Opto-Electronic Route to Nanotechnology. *Opto-electron. Rev.* **2002**, *10*, 217−224.

(3) Liang, Z.; Sun, J.; Jiang, Y.; Jiang, L.; Chen, X. Plasmonic Enhanced Optoelectronic Devices. *Plasmonics* **2014**, *9*, 859−866.

(4) Davis, T. J.; Gómez, D. E.; Roberts, A. Plasmonic Circuits for Manipulating Optical Information. *Nanophotonics* **2017**, *6*, 543−559.

(5) Wei, H.; Wang, Z.; Tian, X.; Käll, M.; Xu, H. Cascaded Logic Gates in Nanophotonic Plasmon Networks. *Nat. Commun.* **2011**, *2*, 387.

(6) Bozhevolnyi, S. I.; Mortensen, N. Plasmonics for Emerging Quantum Technologies. *Nanophotonics* **2017**, *6*, 1185−1188.

(7) Andersen, M. L.; Stobbe, S.; Sørensen, A. S.; Lodahl, P. Strongly Modified Plasmon−Matter Interaction with Mesoscopic Quantum Emitters. *Nat. Phys.* **2011**, *7*, 215−218.

(8) Homola, J.; Yee, S. S.; Gauglitz, G. Surface Plasmon Resonance Sensors: Review. *Sens. Actuators, B* **1999**, *54*, 3−15.

(9) Ray, P. C. Size and Shape Dependent Second Order Nonlinear Optical Properties of Nanomaterials and Their Application in Biological and Chemical Sensing. *Chem. Rev.* **2010**, *110*, 5332−5365.

(10) Hsu, L.-Y.; Ding, W.; Schatz, G. C. Plasmon-Coupled Resonance Energy Transfer. *J. Phys. Chem. Lett.* **2017**, *8*, 2357−2367.

(11) Li, J.; Cushing, S. K.; Meng, F.; Senty, T. R.; Bristow, A. D.; Wu, N. Plasmon-Induced Resonance Energy Transfer for Solar Energy Conversion. *Nat. Photonics* **2015**, *9*, 601−607.

(12) Clavero, C. Plasmon-Induced Hot-Electron Generation at Nanoparticle/Metal-Oxide Interfaces for Photovoltaic and Photocatalytic Devices. *Nat. Photonics* **2014**, *8*, 95−103.

(13) Sundararaman, R.; Narang, P.; Jermyn, A. S.; Goddard, W. A.; Atwater, H. A. Theoretical Predictions for Hot-Carrier Generation from Surface Plasmon Decay. *Nat. Commun.* **2014**, *5*, 5788.

(14) Brongersma, M. L.; Halas, N. J.; Nordlander, P. Plasmon-Induced Hot Carrier Science and Technology. *Nat. Nanotechnol.* **2015**, *10*, 25−34.

(15) García de Abajo, F. J. G. Optical Excitations in Electron Microscopy. *Rev. Mod. Phys.* **2010**, *82*, 209−275.

(16) Wu, Y.; Li, G.; Camden, J. P. Probing Nanoparticle Plasmons with Electron Energy Loss Spectroscopy. *Chem. Rev.* **2018**, *118*, 2994−3031.

(17) Kociak, M.; Stéphan, O.; Gloter, A.; Zagonel, L. F.; Tizei, L. H. G.; Tencé, M.; March, K.; Blazit, J. D.; Mahfoud, Z.; Losquin, A.; Meuret, S.; Colliex, C. Seeing and Measuring in Colours: Electron Microscopy and Spectroscopies Applied to Nano-Optics. *C. R. Phys.* **2014**, *15*, 158−175.

(18) Fischer, M. C.; Wilson, J. W.; Robles, F. E.; Warren, W. S. Invited Review Article: Pump-Probe Microscopy. *Rev. Sci. Instrum.* **2016**, *87*, No. 031101.

(19) Newton, M. C; Parsons, A.; Wagner, U.; Rau, C. Coherent X-Ray Diffraction Imaging of Photo-Induced Structural Changes in Bifeo 3 Nanocrystals. *New J. Phys.* **2016**, *18*, No. 093003.

(20) Shen, X.; Li, R. K.; Lundstrom, U.; Lane, T. J.; Reid, A. H.; Weathersby, S. P.; Wang, X. J. Femtosecond Mega-Electron-Volt Electron Microdiffraction. *Ultramicroscopy* **2018**, *184*, 172−176.

(21) Barwick, B.; Zewail, A. H. Photonics and Plasmonics in 4d Ultrafast Electron Microscopy. *ACS Photonics* **2015**, *2*, 1391−1402.

(22) Shorokhov, D.; Zewail, A. H. Perspective: 4d Ultrafast Electron Microscopy—Evolutions and Revolutions. *J. Chem. Phys.* **2016**, *144*, No. 080901.

(23) Howie, A. New Instrumentation and Cutting Edge Research. *Ultramicroscopy* **2017**, *180*, 52−58.

DOI: 10.1021/acsphotonics.9b00830
ACS Photonics XXXX, XXX, XXX−XXX

(24) Losquin, A.; Lummen, T. T. A. Electron Microscopy Methods for Space-, Energy-, and Time-Resolved Plasmonics. *Front. Phys.* **2017**, *12*, 127301.
(25) Zewail, A. H. Four-Dimensional Electron Microscopy. *Science* **2010**, *328*, 187−193.
(26) Boersch, H.; Geiger, J.; Stickel, W. Interaction of 25-Kev Electrons with Lattice Vibrations in Lif. Experimental Evidence for Surface Modes of Lattice Vibration. *Phys. Rev. Lett.* **1966**, *17*, 379−381.
(27) Lagos, M. J.; Batson, P. E. Electron Energy-Gain Processes in Nanostructures Induced by Fast Electrons. *Microscopy & Microanalysis*; August 2017, St. Louis, MO.
(28) Idrobo, J. C.; Lupini, A. R.; Feng, T.; Unocic, R. R.; Walden, F. S.; Gardiner, D. S.; Lovejoy, T. C.; Dellby, N.; Pantelides, S. T.; Krivanek, O. L. Temperature Measurement by a Nanoscale Electron Probe Using Energy Gain and Loss Spectroscopy. *Phys. Rev. Lett.* **2018**, *120*, No. 095901.
(29) Howie, A. Electrons and Photons: Exploiting the Connection. *IOP Conf. Ser.* **1999**, *161*, 311−314.
(30) Abajo, F. J. G. d.; Kociak, M. Electron Energy-Gain Spectroscopy. *New J. Phys.* **2008**, *10*, No. 073035.
(31) Barwick, B.; Flannigan, D. J.; Zewail, A. H. Photon-Induced near-Field Electron Microscopy. *Nature* **2009**, *462*, 902−906.
(32) Yurtsever, A.; Baskin, J. S.; Zewail, A. H. Entangled Nanoparticles: Discovery by Visualization in 4d Electron Microscopy. *Nano Lett.* **2012**, *12*, 5027−5032.
(33) Pomarico, E.; Madan, I.; Berruto, G.; Vanacore, G. M.; Wang, K.; Kaminer, I.; García de Abajo, F. J.; Carbone, F. Mev Resolution in Laser-Assisted Energy-Filtered Transmission Electron Microscopy. *ACS Photonics* **2018**, *5*, 759−764.
(34) García de Abajo, F. J.; Asenjo-Garcia, A.; Kociak, M. Multiphoton Absorption and Emission by Interaction of Swift Electrons with Evanescent Light Fields. *Nano Lett.* **2010**, *10*, 1859−1863.
(35) Park, S. T.; Lin, M. M.; Zewail, A. H. Photon-Induced near-Field Electron Microscopy (Pinem): Theoretical and Experimental. *New J. Phys.* **2010**, *12*, 123028.
(36) Asenjo-Garcia, A.; García de Abajo, F. J. Plasmon Electron Energy-Gain Spectroscopy. *New J. Phys.* **2013**, *15*, 103021.
(37) Das, P.; Blazit, J. D.; Tencé, M.; Zagonel, L. F.; Auad, Y.; Lee, Y. H.; Ling, X. Y.; Losquin, A.; Colliex, C.; Stéphan, O.; García de Abajo, F. J.; Kociak, M. Stimulated Electron Energy Loss and Gain in an Electron Microscope without a Pulsed Electron Gun. *Ultramicroscopy* **2019**, *203*, 44−51.
(38) Kaplan, M.; Yoo, B.-K.; Tang, J.; Karam, T. E.; Liao, B.; Majumdar, D.; Baltimore, D.; Jensen, G. J.; Zewail, A. H. Photon-Induced near-Field Electron Microscopy of Eukaryotic Cells. *Angew. Chem., Int. Ed.* **2017**, *56*, 11498−11501.
(39) Flannigan, D. J.; Barwick, B.; Zewail, A. H. Biological Imaging with 4d Ultrafast Electron Microscopy. *Proc. Natl. Acad. Sci. U. S. A.* **2010**, *107*, 9933.
(40) Wu, Y.; Liu, C.; Moore, T. M.; Magel, G. A.; Garfinkel, D. A.; Camden, J. P.; Stanford, M. G.; Duscher, G.; Rack, P. D. Exploring Photothermal Pathways Via in Situ Laser Heating in the Transmission Electron Microscope: Recrystallization, Grain Growth, Phase Separation, and Dewetting in Ag0.5ni0.5 Thin Films. *Microsc. Microanal.* **2018**, *24*, 647−656.
(41) Mukamel, S. Causal Versus Noncausal Description of Nonlinear Wave Mixing: Resolving the Damping-Sign Controversy. *Phys. Rev. A: At., Mol., Opt. Phys.* **2007**, *76*, No. 021803.
(42) Bialynicki-Birula, I.; Sowiński, T. Quantum Electrodynamics of Qubits. *Phys. Rev. A: At., Mol., Opt. Phys.* **2007**, *76*, No. 062106.
(43) Masiello, D. J.; Schatz, G. C. Many-Body Theory of Surface-Enhanced Raman Scattering. *Phys. Rev. A: At., Mol., Opt. Phys.* **2008**, *78*, No. 042505.
(44) Purcell, E. M.; Pennypacker, C. R. Scattering and Absorption of Light by Nonspherical Dielectric Grains. *Astrophys. J.* **1973**, *186*, 705−714.
(45) Draine, B. T.; Flatau, P. J. Discrete-Dipole Approximation for Scattering Calculations. *J. Opt. Soc. Am. A* **1994**, *11*, 1491−1499.
(46) Hohenester, U.; Trügler, A. Mnpbem − a Matlab Toolbox for the Simulation of Plasmonic Nanoparticles. *Comput. Phys. Commun.* **2012**, *183*, 370−381.
(47) Bigelow, N. W.; Vaschillo, A.; Camden, J. P.; Masiello, D. J. Signatures of Fano Interferences in the Electron Energy Loss Spectroscopy and Cathodoluminescence of Symmetry-Broken Nanorod Dimers. *ACS Nano* **2013**, *7*, 4511−4519.
(48) Bigelow, N. W.; Vaschillo, A.; Iberi, V.; Camden, J. P.; Masiello, D. J. Characterization of the Electron- and Photon-Driven Plasmonic Excitations of Metal Nanorods. *ACS Nano* **2012**, *6*, 7497−7504.

DOI: 10.1021/acsphotonics.9b00830
ACS Photonics XXXX, XXX, XXX−XXX